

Piezoelectric altermagnetism and spin-valley polarization in Janus monolayer Cr₂SO

San-Dong Guo¹, Xiao-Shu Guo¹, Kai Cheng¹, Ke Wang¹ and Yee Sin Ang²

¹*School of Electronic Engineering, Xi'an University of Posts and Telecommunications, Xi'an 710121, China and*

²*Science, Mathematics and Technology (SMT), Singapore University of Technology and Design (SUTD), 8 Somapah Road, Singapore 487372, Singapore*

The altermagnetism can achieve spin-split bands in collinear symmetry-compensated antiferromagnets. Here, we predict altermagnetic order in Janus monolayer Cr₂SO with eliminated inversion symmetry, which can realize the combination of piezoelectricity and altermagnetism in a two-dimensional material, namely 2D piezoelectric altermagnetism. It is found that Cr₂SO is an altermagnetic semiconductor, and the spin-split bands of both valence and conduction bands are near the Fermi level. The Cr₂SO has large out-of-plane piezoelectricity ($|d_{31}|=0.97$ pm/V), which is highly desirable for ultrathin piezoelectric device application. Due to spin-valley locking, both spin and valley can be polarized by simply breaking the corresponding crystal symmetry with uniaxial strain. Our findings provide a platform to integrate spin, piezoelectricity and valley in a single material, which is useful for multi-functional device applications.

Keywords: Altermagnetism, Spin-split bands, Valley, Strain

Email:sandongyuwang@163.com

INTRODUCTION

The antiferromagnetic (AFM) materials do not have any net magnetic moment, which are robust to external magnetic perturbation, and have ultra-high dynamic speed, allowing high-speed device operation[1, 2]. However, it is often hard to realize spin-polarized currents in collinear AFM systems because of the missing spin-splitting in the band structures[3]. Recently, the spin-splitting has been achieved in collinear symmetry-compensated antiferromagnets, be called altermagnetism[4–6]. The spin-splitting is only originated from the simple AFM order with special magnetic space group, and the relativistic spin-orbital coupling (SOC) is thus not needed. Several bulk materials have been predicted to be altermagnetism, such as RuO₂[7], FeF₂[8], MnTe[9], some organic AFMs[10], MnF₂[11] and some GdFeO₃-type perovskites[12].

Besides, several two-dimensional (2D) materials have also been predicted to have this spin-splitting with special AFM order, such as Cr₂O₂[13, 14] and V₂Se₂O[15]. However, these 2D altermagnetic materials have inversion symmetry, leading to missing piezoelectricity. Searching for 2D piezoelectric altermagnetism (PAM) may be significative and challenging. In fact, many 2D piezoelectric ferromagnetisms (PFMs) has been predicted[16–20], which achieve the combination of piezoelectricity and ferromagnetic (FM) order in a 2D material. Most of these 2D PFMs possess Janus structure, which can destroy out-of-plane symmetry, inducing out-of-plane piezoelectricity. Therefore, 2D Janus materials may provide a potential platform for searching 2D PAMs. Another question is how to achieve spin polarization in 2D altermagnetic materials, and strain may be a very effective way to induce spin polarization[13–15].

Here, we construct Janus monolayer Cr₂SO as derivative of altermagnetic Cr₂O₂ monolayer. Calculated re-

sults show that Cr₂SO is still a 2D altermagnetic material, and has large out-of-plane piezoelectricity, which achieves PAM. Both spin and valley polarizations can be realized by simply breaking the corresponding crystal symmetry with uniaxial strain. Compared with existing 2D altermagnetic Cr₂O₂[13, 14] and V₂Se₂O[15], Cr₂SO has two main differences: (1) it has large out-of-plane piezoelectricity; (2) near the Fermi level, the states of conduction and valence bands around X or Y high-symmetry point are with opposite spins.

COMPUTATIONAL DETAIL

We perform the spin-polarized first-principles calculations within density functional theory (DFT)[21] by using the standard VASP package[22–24] within the projector augmented-wave (PAW) method. The generalized gradient approximation of Perdew-Burke-Ernzerhof (PBE-GGA)[25] is used as the exchange-correlation functional. We set kinetic energy cutoff of 500 eV, total energy convergence criterion of 10⁻⁸ eV, and force convergence criterion of 0.0001 eV.Å⁻¹. To account for electron correlation of Cr-3d orbitals, a Hubbard correction $U_{eff}=3.55$ eV[13, 14] is employed within the rotationally invariant approach proposed by Dudarev et al. The out-of-plane interaction is avoided by taking a vacuum of more than 16 Å. We use a 18×18×1 Monkhorst-Pack k-point meshes to sample the Brillouin zone (BZ) for calculating electronic structures, elastic and piezoelectric properties.

The elastic stiffness tensor C_{ij} are calculated by using strain-stress relationship (SSR) method. The piezoelectric stress tensor e_{ij} are calculated by density functional perturbation theory (DFPT) method[26]. The C_{ij}^{2D}/e_{ij}^{2D} have been renormalized by $C_{ij}^{2D}=L_z C_{ij}^{3D}/e_{ij}^{2D}=L_z e_{ij}^{3D}$, where the L_z is the length of unit cell along z direction. Based on finite displacement method, the interatomic force constants (IFCs) are calculated by using

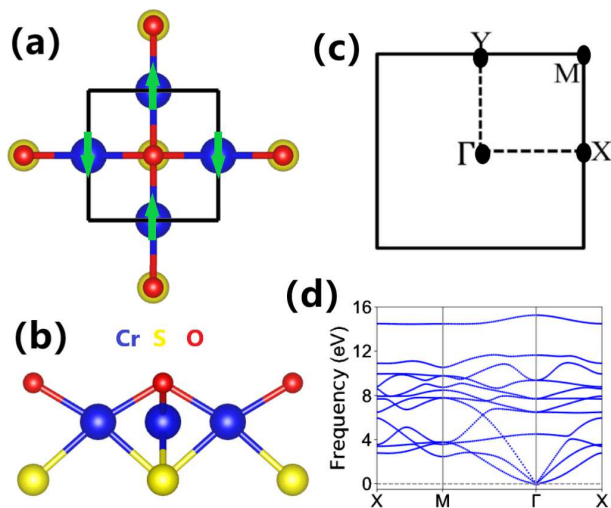


FIG. 1. (Color online) For Janus monolayer Cr_2SO , (a) and (b): top and side views of the crystal structures; (c): The first BZ with high symmetry points; (d): the phonon dispersion curves.

$5 \times 5 \times 1$ supercell, and the phonon dispersion spectrum is obtained by the Phonopy code[27]. The ab-initio molecular dynamics (AIMD) simulations using NVT ensemble are performed for more than 8000 fs with a time step of 1 fs by using a $4 \times 4 \times 1$ supercell. The elastic, piezoelectric, phonon and AIMD calculations are all carried out with altermagnetic order.

CRYSTAL STRUCTURE AND STABILITY

Monolayer Cr_2SO and Cr_2O_2 have similar crystal structures, and they contain three atomic sublayers with two co-planar Cr atoms as middle layer and O/S atoms as upper and lower layers. The Janus monolayer Cr_2SO can be constructed by replacing one of two O layers with S atoms in monolayer Cr_2O_2 . The schematic crystal structures of Cr_2SO are shown in Figure 1 (a) and (b). The monolayer Cr_2O_2 possesses $P4/mmm$ space group (No.123)[13, 14], and the monolayer Cr_2SO crystallizes in the $P4mm$ space group (No.99). For monolayer Cr_2O_2 , the key space-group symmetry operations contain space inversion P , C_4 rotation and $M_x/M_y/M_z/M_{xy}$ mirror, indicating no piezoelectricity. With respect to Cr_2O_2 , the P and M_z of Cr_2SO are removed, which means that the Cr_2SO will be piezoelectric. In one unit cell, the FM and AFM configurations are constructed to determine magnetic ground state and lattice constants. Calculated results show that the AFM configuration is ground state of Cr_2SO , and its energy is 1.122 eV lower than that of FM case within GGA+ U . The optimized lattice constants $a=b=3.66 \text{ \AA}$ by GGA+ U for AFM case. The magnetic easy-axis is investigated by calculating the energy difference of the magnetization orientation along the (100)

and (001) cases, which is defined as magnetic anisotropy energy (MAE). Calculated results show that the MAE is $-93 \mu\text{eV}/\text{Fe}$, which indicates that the easy-axis of Cr_2SO is in-plane.

To evaluate the stability of Cr_2SO , the phonon dispersion, molecular dynamics and elastic constants are calculated by using GGA+ U for AFM case. The phonon dispersions of Cr_2SO are shown in Figure 1 (d), and no imaginary frequencies can be observed, indicating its dynamic stability. To corroborate the thermal stability, the evolution of total energy vs time are calculated using AIMD at 200 and 300 K, which are shown in FIG.1 and FIG.2 of electronic supplementary information (ESI). At 200 K, the energies are kept stable, and the crystal features are preserved after 8 ps, which confirms its thermal stability. However, at 300 K, the thermal stability of Cr_2SO is broken. The independent elastic constants C_{11} , C_{12} and C_{66} of Cr_2SO are 64.93 Nm^{-1} , 37.26 Nm^{-1} and 30.05 Nm^{-1} , which satisfy the Born criteria of mechanical stability: $C_{11} > 0$, $C_{66} > 0$, $C_{11} - C_{12} > 0$, confirming its mechanical stability.

ELECTRONIC STRUCTURES

The planar average of the electrostatic potential energy along out-of-plane direction is shown in Figure 2 (a). Due to mirror asymmetry, an electrostatic potential gradient ($\Delta\Phi$) of about 0.28 eV is produced, which is related to the work function change of the structure. Due to the electron redistribution, there is an inherent electric field with the magnitude of about 5.73 V/\AA , implying a very strong vertical polarization in the Cr_2SO monolayer.

The Cr atoms in Cr_2SO monolayer possess a local magnetic moment around $3.46 \mu_B$, and the two Cr-atom sublattices with the 2D Néel AFM order are related by M_{xy} mirror symmetry but cannot be transformed to each other by any translation operation, which leads to existing altermagnetism. The energy band structures of Cr_2SO are plotted in Figure 2 (b) by GGA+ U method without SOC. There are two valleys at X and Y high-symmetry points for both conduction and valence bands, which are related by the mirror symmetry. States around X and Y points are mainly from two different Cr atoms with opposite spins due to the Néel AFM order, producing altermagnetism in the absence of SOC and spin-valley locking. Compared with spin-gapless Cr_2O_2 [13, 14], it is clearly seen that Cr_2SO is a direct band gap semiconductor with gap value of 0.838 eV, which may be due to strong inherent electric field ($\sim 5.73 \text{ V/\AA}$). The valence band maximum (VBM) and conduction band bottom (CBM) of Cr_2SO are at high symmetry X or Y point, while those of Cr_2O_2 deviate from X or Y point. Near the Fermi level, states of conduction and valence bands around X or Y point are from two different Cr atoms with opposite spins, while those of Cr_2O_2 are with the same

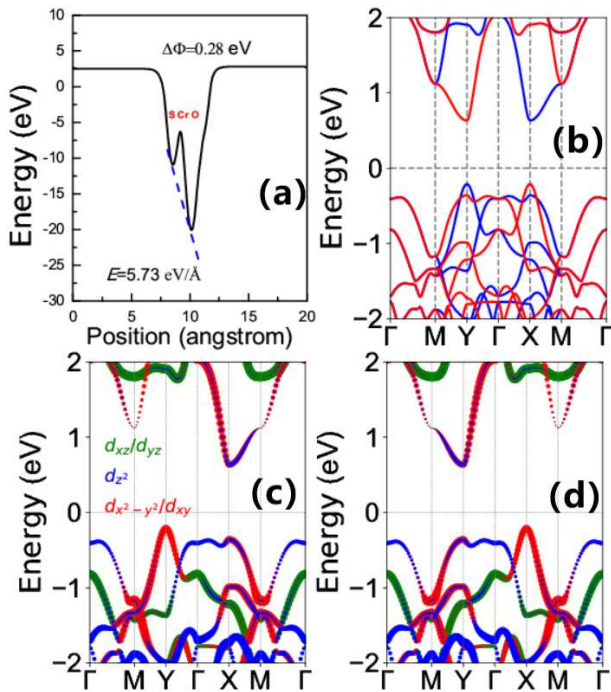


FIG. 2. (Color online) For Cr_2SO , (a): planar averaged electrostatic potential energy variation along z direction. $\Delta\phi$ is the potential energy difference across the layer. E stands for the intrinsic polar field; (b): the energy band structures. The spin-up and spin-down channels are depicted in blue and red; (c) and (d): the Cr- d -resolved band structures for spin-up and spin-down channels.

spins[13, 14]. For $\text{V}_2\text{Se}_2\text{O}$ monolayer, the same spins are also observed for states of conduction and valence bands around X or Y point near the Fermi level[15]. According to Figure 2 (b) and (d), it is found that $d_{x^2-y^2} + d_{xy} + d_{z^2}$ orbitals dominate X and Y valleys of conduction bands, and the X and Y valleys of valence bands are mainly from $d_{x^2-y^2} + d_{xy}$ orbitals.

The electronic correlation effects on electronic structures of Cr_2SO are considered by using different U values. Firstly, the lattice constants a at different U (0-4 eV) are optimized, and then calculate electronic properties of Cr_2SO . With increasing U , the lattice constants a increases, and its change is about 0.232 Å. According to FIG.3 of ESI, it is found that Cr_2SO is always a AFM ground state. The evolutions of energy band structures as a function of U are calculated, which are plotted in FIG.4 of ESI. With increasing the U , monolayer Cr_2SO experiences a phase transition from metal to semiconductor, and the critical point is about 2 eV. Similar phenomenon can be also observed in monolayer $\text{V}_2\text{Se}_2\text{O}$ [15]. For $U \geq 2$ eV, near the Fermi level, states of conduction and valence bands around X or Y point are always from two different Cr atoms with opposite spins.

PIEZOELECTRIC PROPERTIES

Due to inversion symmetry, the Cr_2O_2 monolayer possesses no piezoelectricity. However, the monolayer Cr_2SO has piezoelectricity with missing P and M_z symmetries. Namely, the reflectional symmetry of Cr_2SO disappears across the xy plane, but holds across the xz or yz plane, which leads to existing out-of-plane piezoelectricity and missing in-plane piezoelectricity. The third-rank piezoelectric stress tensor e_{ijk} and strain tensor d_{ijk} can be used to describe the piezoelectric response of a material. They can be expressed as the sum of ionic and electronic contributions:

$$\begin{aligned} e_{ijk} &= \frac{\partial P_i}{\partial \varepsilon_{jk}} = e_{ijk}^{elc} + e_{ijk}^{ion} \\ d_{ijk} &= \frac{\partial P_i}{\partial \sigma_{jk}} = d_{ijk}^{elc} + d_{ijk}^{ion} \end{aligned} \quad (1)$$

Where P_i , ε_{jk} and σ_{jk} are polarization vector, strain and stress, respectively. The superscripts *elc* and *ion* mean electronic and ionic contributions. The e_{ijk}^{elc} and d_{ijk}^{elc} (e_{ijk} and d_{ijk}) are also called clamped-ion (relaxed-ion) piezoelectric coefficients. The e_{ijk} is related with d_{ijk} by elastic tensor C_{mnmjk} :

$$e_{ijk} = \frac{\partial P_i}{\partial \varepsilon_{jk}} = \frac{\partial P_i}{\partial \sigma_{mn}} \cdot \frac{\partial \sigma_{mn}}{\partial \varepsilon_{jk}} = d_{imn} C_{mnmjk} \quad (2)$$

By using Voigt notation, only considering the in-plane strain and stress[28], the Equation 2 can be reduced into:

$$\begin{pmatrix} 0 & 0 & 0 \\ 0 & 0 & 0 \\ e_{31} & e_{31} & 0 \end{pmatrix} = \begin{pmatrix} 0 & 0 & 0 \\ 0 & 0 & 0 \\ d_{31} & d_{31} & 0 \end{pmatrix} \begin{pmatrix} C_{11} & C_{12} & 0 \\ C_{12} & C_{11} & 0 \\ 0 & 0 & C_{66} \end{pmatrix} \quad (3)$$

The existing e_{31}/d_{31} means that only vertical piezoelectric polarization can be induced, when a uniaxial strain is applied. By solving the Equation 3, the d_{31} can be obtained:

$$d_{31} = \frac{e_{31}}{C_{11} + C_{12}} \quad (4)$$

The primitive cell is used to calculate the e_{31} of monolayer Cr_2SO . The calculated e_{31} is -0.987×10^{-10} with ionic part 0.111×10^{-10} and electronic part -1.098×10^{-10} . The electronic and ionic contributions have opposite signs, and the electronic part dominates the piezoelectricity. And then, the d_{31} can be attained from Equation 4, and the corresponding value is -0.97 pm/V. The minus sign depends on the choice of coordinate system. If the $\pm z$ directions are reversed, the d_{31} will become 0.97 pm/V. A large out-of-plane piezoelectric response (d_{31}) is very important to be compatible with the nowadays bottom/top gate technologies. The $|d_{31}|$ of Cr_2SO is compared with or higher than ones of many known 2D materials, like functionalized h-BN (0.13 pm/V)[29],

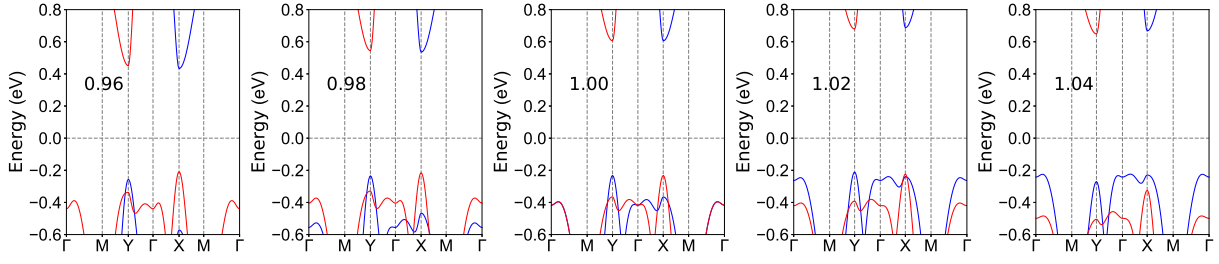


FIG. 3. (Color online) The energy band structures of Cr_2SO at representative a/a_0 . The compressive strain makes X and Y valleys of both conduction and valence bands separate from other bands.

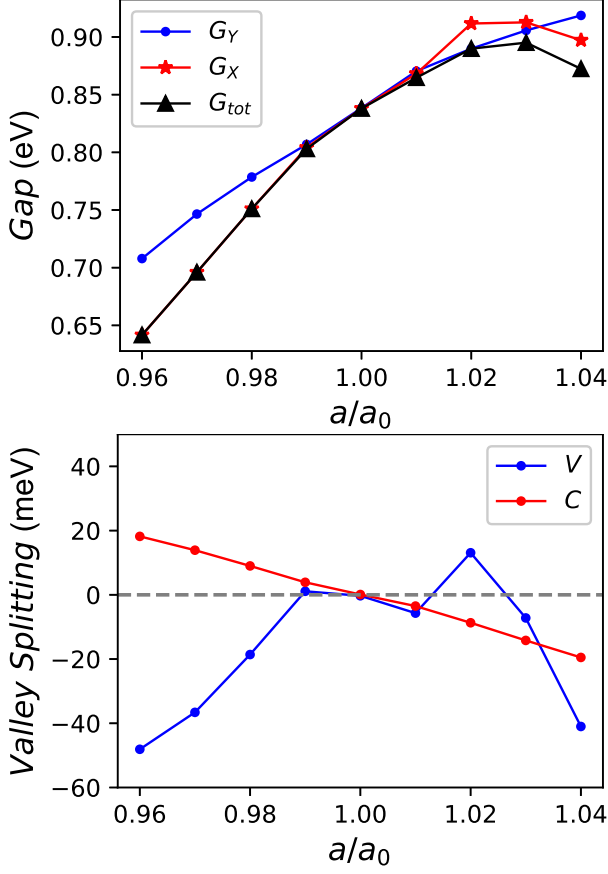


FIG. 4. (Color online) For Cr_2SO , the related band gaps including the global gap [G_{tot}] and gaps of Y and X valleys [G_Y and G_X] (top panel), and valley splitting for both valence [V] and conduction [C] bands (bottom panel) as a function of a/a_0 .

kalium decorated graphene (0.3 pm/V)[28], the oxygen functionalized MXenes (0.40-0.78 pm/V)[30], Janus group-III materials (0.46 pm/V)[31], Janus BiTeI/SbTeI monolayer (0.37-0.66 pm/V)[32], Janus monolayer transition metal dichalcogenides (0.03 pm/V)[33] and $\alpha\text{-In}_2\text{Se}_3$ (0.415 pm/V)[34]. The large $|d_{31}|$ may be related to large electronegativity difference of S and O atoms[19, 20]. The large $|d_{31}|$ provide possibility to tune spin-split bands of alternating Cr_2SO by piezoelectric effect.

UNIAXIAL STRAIN INDUCES SPIN-VALLEY POLARIZATION

To induce spin-valley polarization in Cr_2SO , an experimentally feasible approach is to destroy M_{xy} symmetry by applying uniaxial strain along x or y direction, which will lead to nonequivalent X and Y valleys, giving rise to spin-valley polarization. We use a/a_0 (0.96 to 1.04) to simulate the uniaxial strain along x direction, and the lattice constants b along y direction is optimized. The a and a_0 are the strained and unstrained lattice constants with $a/a_0 < 1$ ($a/a_0 > 1$) being compressive (tensile) case. If the strain is applied along y direction, the opposite gap change and spin-valley polarization are exactly generated, since two valleys are related with M_{xy} symmetry. The Young's modulus is calculated to elucidate mechanical performance of Cr_2SO , which is plotted in FIG.5 of ESI. The calculated C_{2D} of Cr_2SO along x direction (44 Nm^{-1}) is very small than those of many known 2D materials, such as graphene ($\sim 340 \pm 40 \text{ Nm}^{-1}$) and MoS_2 ($\sim 126.2 \text{ Nm}^{-1}$) [35, 36], indicating its better mechanical flexibility.

The energy differences (ΔE) between AFM and FM states vs a/a_0 are calculated to determine the magnetic ground state of strained Cr_2SO , which are plotted in FIG.6 of ESI. Within considered strain range, the ΔE is always negative, confirming that strained Cr_2SO is AFM ground state. The energy band structures of strained monolayer Cr_2SO are shown in Figure 3. The evolutions of related energy band gap (global gap [G_{tot}] and gaps of Y and X valleys [G_Y and G_X]) and the valley splitting ($\Delta E_C = E_Y^C - E_X^C$ and $\Delta E_V = E_Y^V - E_X^V$) for both valence and conduction bands as a function of a/a_0 are plotted in Figure 4. For unstrained case, the global gap and gaps of X and Y valleys are the same, indicating no valley polarization. It is found that both compressive and tensile strains can induce unequal gap between X and Y valleys, which can produce valley polarization for both conduction and valence bands. It is clearly seen that compressive strain is in favour of separating X and Y valleys of both conduction and valence bands from other bands, which makes for easily manipulating these valleys in experiment. At $a/a_0=0.96$, the corresponding valley

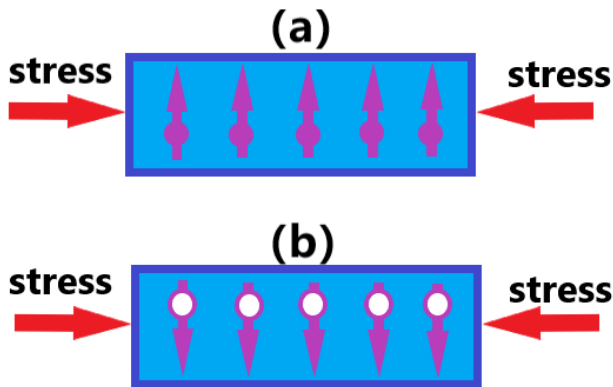


FIG. 5. (Color online) For Cr_2SO with compressive strain, an appropriate electron/hole doping leads to that only one valley has doped electron/holes. Due to spin-valley locking, the electron carriers possess spin-up character (a), while hole carriers have spin-down one (b).

splitting are 18 meV (-48 meV) for conduction (valence) band.

For compressive strain, an appropriate electron/hole doping can move the Fermi level to fall between the X and Y valleys, which leads to that only one valley has doped electron/holes. Due to spin-valley locking (see Figure 3 and Figure 5), the electron carriers possess spin-up character, while hole carriers have spin-down one. Upon appropriate doping, the magnetization can be produced due to the polarized carriers. The electron and hole doping leads to opposite magnetization direction. For a given electron/hole density, the magnetization can be tuned by uniaxial strain. These provide a platform for spin device applications.

CONCLUSION

In summary, we propose a 2D Janus altermagnetic material Cr_2SO , which is dynamically, mechanically and thermally stable. Calculated results show that Cr_2SO is a semiconductor with spin-split bands near the Fermi level. The structural symmetry-breaking and large electronegativity difference of O and S atoms lead to a large out-of-plane piezoelectric coefficient ($|d_{31}|$) of 0.97 pm/V. The Cr_2SO possesses spin-valley locking, which is comprised of spin-polarized valleys related by a crystal symmetry. The spin-valley polarization can be induced by simply breaking the corresponding crystal symmetry with uniaxial strain. In fact, we provide a very effective method to induce piezoelectricity from centrosymmetric altermagnetism by constructing Janus structure. The method, analysis and results can be readily extended to other members of centrosymmetric monolayer altermagnetism AB (A = Co, Cr, Fe, Mn, Mo, Nb, Ni, Pd, Rh, Ru, Sc, Ti, V, Y, Zr; B = B, C, N, O, F, Al, Si, P, S, Cl, Ga, Ge, As, Se, Br), possessing the same structure and AFM

magnetic configuration with Cr_2O_2 [13]. Based on these altermagnetic monolayers, constructing Janus structure can realize piezoelectric altermagnetism.

This work is supported by Natural Science Basis Research Plan in Shaanxi Province of China (2021JM-456). We are grateful to Shanxi Supercomputing Center of China, and the calculations were performed on TianHe-2..

-
- [1] X. Hu, *Adv. Mater.* **24**, 294 (2012).
 - [2] T. Jungwirth, J. Sinova, A. Manchon, X. Marti, J. Wunderlich and C. Felser, *Nat. Phys.* **14**, 200 (2018).
 - [3] J. Železný, Y. Zhang, C. Felser and B. Yan, *Phys. Rev. Lett.* **119**, 187204 (2017).
 - [4] L. Šmejkal, J. Sinova and T. Jungwirth, *Phys. Rev. X* **12**, 031042 (2022).
 - [5] I. Mazin *Phys. Rev. X* **12**, 040002 (2022).
 - [6] L. Šmejkal, J. Sinova and T. Jungwirth, *Phys. Rev. X* **12**, 040501 (2022).
 - [7] L. Šmejkal, R. González-Hernández, T. Jungwirth and J. Sinova, *Sci. Adv.* **6**, eaaz8809 (2020).
 - [8] S. López-Moreno, A. H. Romero, J. Mejía-López, A. Muñoz and Igor V. Roshchin, *Phys. Rev. B* **85**, 134110 (2012).
 - [9] I. I. Mazin, *Phys. Rev. B* **107**, L100418 (2023).
 - [10] M. Naka, S. Hayami, H. Kusunose, Y. Yanagi, Y. Motome and H. Seo, *Nat. Commun.* **10**, 4305 (2019).
 - [11] L.-D. Yuan, Z. Wang, J.-W. Luo, E. I. Rashba and A. Zunger, *Phys. Rev. B* **102**, 014422 (2020).
 - [12] M. Naka, Y. Motome and H. Seo, *Phys. Rev. B* **103**, 125114 (2021).
 - [13] X. Chen, D. Wang, L. Y. Li and B. Sanyal, Preprint at <https://arxiv.org/abs/2104.07390> (2021).
 - [14] P. J. Guo, Z. X. Liu and Z. Y. Lu, *npj Comput. Mater.* **9**, 70 (2023).
 - [15] H.-Y. Ma, M. L. Hu, N. N. Li, J. P. Liu, W. Yao, J. F. Jia and J. W. Liu, *Nat. Commun.* **12**, 2846 (2021).
 - [16] G. Song, C. F. Zhang, Z. Z. Zhang, G. N. Li, Z. W. Li, J. Du, B. W. Zhang, X. K. Huang and B. L. Gao, *Phys. Chem. Chem. Phys.* **24**, 1091 (2022).
 - [17] S. D. Guo, X. S. Guo, X. X. Cai, W. Q. Mu and W. C. Ren, *J. Appl. Phys.* **129**, 214301 (2021).
 - [18] G. Song, D. S. Li, H. F. Zhou et al., *Appl. Phys. Lett.* **118**, 123102 (2021).
 - [19] S. D. Guo, Y. T. Zhu, K. Qin and Y. S. Ang, *Appl. Phys. Lett.* **120**, 232403 (2022).
 - [20] S. D. Guo, X. S. Guo, Y. T. Zhu and Y. S. Ang, *Appl. Phys. Lett.* **121**, 062403 (2022).
 - [21] P. Hohenberg and W. Kohn, *Phys. Rev.* **136**, B864 (1964); W. Kohn and L. J. Sham, *Phys. Rev.* **140**, A1133 (1965).
 - [22] G. Kresse, *J. Non-Cryst. Solids* **193**, 222 (1995).
 - [23] G. Kresse and J. Furthmüller, *Comput. Mater. Sci.* **6**, **15** (1996).
 - [24] G. Kresse and D. Joubert, *Phys. Rev. B* **59**, 1758 (1999).
 - [25] J. P. Perdew, K. Burke and M. Ernzerhof, *Phys. Rev. Lett.* **77**, 3865 (1996).
 - [26] X. Wu, D. Vanderbilt and D. R. Hamann, *Phys. Rev. B* **72**, 035105 (2005).

- [27] A. Togo, F. Oba and I. Tanaka, *Phys. Rev. B* **78**, 134106 (2008).
- [28] M. T. Ong and E. J. Reed, *ACS Nano* **6**, 1387 (2012).
- [29] A. A. M. Noor, H. J. Kim and Y. H. Shin, *Phys. Chem. Chem. Phys.* **16**, 6575 (2014).
- [30] J. Tan, Y. H. Wang, Z. T. Wang, X. J. He, Y. L. Liu, B. Wanga, M. I. Katsnelson and S. J. Yuan, *Nano Energy* **65**, 104058 (2019).
- [31] Y. Guo, S. Zhou, Y. Z. Bai, and J. J. Zhao, *Appl. Phys. Lett.* **110**, 163102 (2017).
- [32] S. D. Guo, X. S. Guo, Z. Y. Liu and Y. N. Quan, *J. Appl. Phys.* **127**, 064302 (2020).
- [33] L. Dong, J. Lou and V. B. Shenoy, *ACS Nano*, **11**, 8242 (2017).
- [34] L. Hu and X.R. Huang, *RSC Adv.* **7**, 55034 (2017).
- [35] K. N. Duerloo, M. T. Ong and E. J. Reed, *J. Phys. Chem. Lett.* **3**, 2871 (2012).
- [36] C. Lee, X. g Wei, J. W. Kysar and J. Hone, *Science* **321**, 385 (2008).